

ACCEPTED MANUSCRIPT • OPEN ACCESS

## Nonlinear localized modes in two-dimensional hexagonally-packed magnetic lattices

To cite this article before publication: Christopher Chong *et al* 2021 *New J. Phys.* in press <https://doi.org/10.1088/1367-2630/abdb6f>

### Manuscript version: Accepted Manuscript

Accepted Manuscript is "the version of the article accepted for publication including all changes made as a result of the peer review process, and which may also include the addition to the article by IOP Publishing of a header, an article ID, a cover sheet and/or an 'Accepted Manuscript' watermark, but excluding any other editing, typesetting or other changes made by IOP Publishing and/or its licensors"

This Accepted Manuscript is © 2020 The Author(s). Published by IOP Publishing Ltd on behalf of Deutsche Physikalische Gesellschaft and the Institute of Physics.

As the Version of Record of this article is going to be / has been published on a gold open access basis under a CC BY 3.0 licence, this Accepted Manuscript is available for reuse under a CC BY 3.0 licence immediately.

Everyone is permitted to use all or part of the original content in this article, provided that they adhere to all the terms of the licence <https://creativecommons.org/licenses/by/3.0>

Although reasonable endeavours have been taken to obtain all necessary permissions from third parties to include their copyrighted content within this article, their full citation and copyright line may not be present in this Accepted Manuscript version. Before using any content from this article, please refer to the Version of Record on IOPscience once published for full citation and copyright details, as permissions may be required. All third party content is fully copyright protected and is not published on a gold open access basis under a CC BY licence, unless that is specifically stated in the figure caption in the Version of Record.

View the [article online](#) for updates and enhancements.

# Nonlinear Localized Modes in Two-Dimensional Hexagonally-Packed Magnetic Lattices

C. Chong\*,<sup>1</sup> Yifan Wang,<sup>2</sup> Donovan Maréchal,<sup>2</sup> E. G. Charalampidis,<sup>3</sup> Miguel Molerón,<sup>4</sup>  
Alejandro J. Martínez,<sup>5,6</sup> Mason A. Porter,<sup>7</sup> P. G. Kevrekidis,<sup>8</sup> and Chiara Daraio<sup>2</sup>

<sup>1</sup>*Department of Mathematics, Bowdoin College, Brunswick, ME 04011, USA*

<sup>2</sup>*Division of Engineering and Applied Science California Institute of Technology Pasadena, CA 91125, USA*

<sup>3</sup>*Mathematics Department, California Polytechnic State University, San Luis Obispo, CA 93407-0403, USA*

<sup>4</sup>*Institute of Geophysics, Department of Earth Sciences, ETH Zurich, 8092 Zurich, Switzerland*

<sup>5</sup>*Computational Biology Laboratory, Fundación Ciencia & Vida, Santiago, 7780272, Chile*

<sup>6</sup>*Universidad San Sebastian, Santiago, 7510156, Chile*

<sup>7</sup>*Department of Mathematics, University of California, Los Angeles, CA 90095, USA*

<sup>8</sup>*Department of Mathematics and Statistics, University of Massachusetts, Amherst, MA, 01003, USA*

We conduct an extensive study of nonlinear localized modes (NLMs), which are temporally periodic and spatially localized structures, in a two-dimensional array of repelling magnets. In our experiments, we arrange a lattice in a hexagonal configuration with a light-mass defect, and we harmonically drive the center of the chain with a tunable excitation frequency, amplitude, and angle. We use a damped, driven variant of a vector Fermi–Pasta–Ulam–Tsingou lattice to model our experimental setup. Despite the idealized nature of this model, we obtain good qualitative agreement between theory and experiments for a variety of dynamical behaviors. We find that the spatial decay is direction-dependent and that drive amplitudes along fundamental displacement axes lead to nonlinear resonant peaks in frequency continuations that are similar to those that occur in one-dimensional damped, driven lattices. However, driving along other directions leads to the creation of asymmetric NLMs that bifurcate from the main solution branch, which consists of symmetric NLMs. When we vary the drive amplitude, we observe such behavior both in our experiments and in our simulations. We also demonstrate that solutions that appear to be time-quasiperiodic bifurcate from the branch of symmetric time-periodic NLMs.

## I. INTRODUCTION

Discrete breathers are spatially localized, time-periodic solutions of nonlinear lattice differential equations. They have been studied in a host of scientific areas, including optical waveguide arrays and photorefractive crystals [1], Josephson-junction ladders [2, 3], layered antiferromagnetic crystals [4, 5], halide-bridged transition-metal complexes [6], dynamical models of the DNA double strand [7], molecular lattices [8], Bose–Einstein condensates in optical lattices [9], and many others.

Most of the immense volume of work — now spanning more than three decades — on discrete breathers has been in one-dimensional (1D) lattices [10–12]. Most relevant to the present article is research on discrete breathers in Fermi–Pasta–Ulam–Tsingou (FPUT) lattices, which have nonlinear inter-site coupling [13, 14]. Additionally, FPUT-like lattices with power-law potentials have been used to model a variety of mechanical systems, such as granular crystals [15–18] and (more recently) magnetic lattices [19–21].

There have also been some studies of breathers in two-dimensional (2D) lattices, although there are many fewer such studies than of 1D lattices. There are even fewer studies of in-plane breathers [22]. Example 2D physical settings in which breathers have been examined include crystal lattices [12, 23], electric circuits [24], and dusty plasmas [25, 26]. Breathers in 2D lattices have been analyzed with both asymptotic methods [27] and numerical methods in both homogeneous [22, 28] and heterogeneous media [29, 30]. See [8, 31] for overviews of results about 2D breathers.

The 2D setting of the present work is a mechanical system in which each magnet has two in-plane displacement fields, which distinguishes it from many studies of scalar 2D lattices, such as those that describe electrical circuits [24]. Specifically, we examine a lattice of repelling magnets that are arranged in a hexagonal configuration. The choice of a hexagonal arrangement is motivated by our experimental setup, as hexagonal configurations are more robust structurally than other arrangements (such as square configurations). At the center of the lattice is a light-mass defect, which introduces a localized defect mode into the spectrum of the linearization of the system. To excite the system experimentally, we drive the center of the lattice by a force that results from the current that flows along a wire that we suspend above the lattice. We model damping using a dashpot term. Putting everything together, the proposed model for the experimental setup is a damped, driven variant of a vector FPUT lattice.

Although a breather is defined as a spatially localized and time-periodic structure, it is useful to label different types of breathers. Linear systems with an impurity or a defect (e.g., with a particle of lighter mass than the other particles) have isolated points in their spectra that lie above the spectral edge. We call these modes “defect localized modes” [32]. In the presence of nonlinearity, breathers can bifurcate from these modes and can exist for frequencies other than the linear defect frequency. We study such breathers in the present work, and we use the term “nonlinear localized modes” (NLMs) [33] for breathers that manifest in this way. (Such solutions have also been called “defect breathers” in other settings [34].) By contrast, we use the term “intrinsic localized modes” (ILMs) for breathers that do not manifest via a defect or an impurity. One way for ILMs, which we do not investigate in the present paper, to manifest is via a modulation instability of plane waves [10]. In addition to breathers, other kinds of orbits — such as quasiperiodic and chaotic ones — can also occur in nonlinear lattices. For example, such orbits

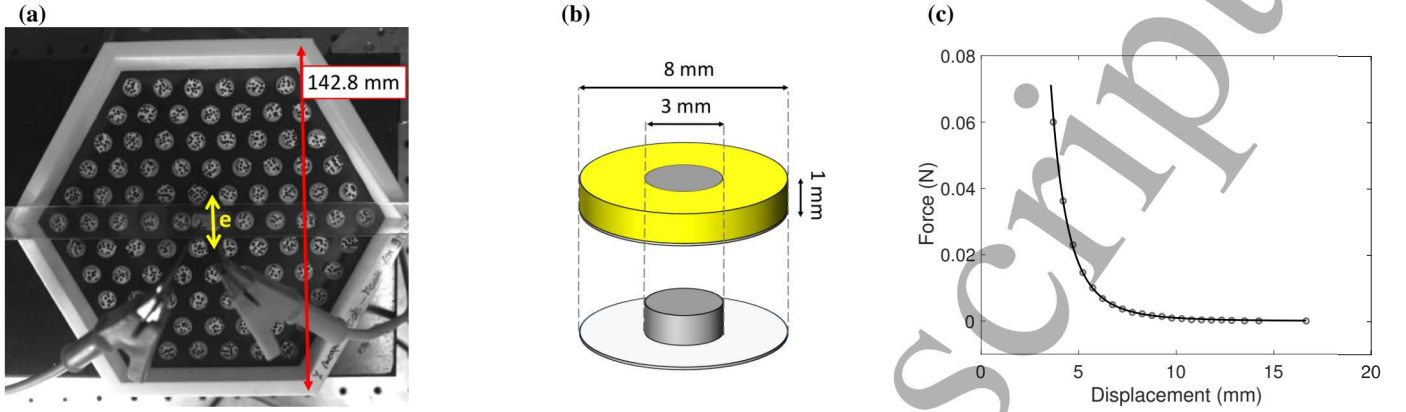


FIG. 1: (a) Picture (from a video frame that was used for particle motion tracking) of our experimental setup. The yellow arrow indicates the direction of the external excitation. (b) Sketches of the (top) normal and (bottom) defect particles. (c) Magnetic dipole–dipole interactions in experiments (open gray circles) and fitted model using Eq. (2) (solid black curve).

have been identified in strongly nonlinear damped, driven granular chains [35, 36], suggesting that such solutions may also be present in damped, driven magnetic lattices. In the present work, we examine such NLM states, their stability, and the modes that arise as a result of instabilities.

Our paper proceeds as follows. We present our experimental setup in Sec. II, and we detail the corresponding model equations, linear theory, and numerical methods in Sec. III. We give the main numerical and experimental results in Sec. IV, where we explore NLM profiles, spatial decay, parameter continuations, and nearly time-quasiperiodic orbits. We conclude and discuss future challenges in Sec. V.

## II. EXPERIMENTAL SETUP

We place a 2D lattice on an air-bearing table to make the magnetic particles (which constitute the nodes of the lattice) levitate. The lattice consists of 127 magnetic particles that are hexagonally packed. We glue 36 of these particles to the boundaries, and 91 of them are free to move [see Fig. 1(a)]. Each particle is a 3D-printed disk with a hole in the center, where we attach a neodymium magnetic cylinder. We glue a thin piece of cover glass at the bottom to make the surface smoother and thereby improve the levitation of the particles. We build the defect particle, which is located in the center of the lattice, by directly attaching the magnet on the glass without the 3D-printed structure. This particle has a lighter mass and serves as a defect [see Fig. 1(b)]. The mean mass of a normal disk particle is  $138.2 \text{ mg} \pm 3.1 \text{ mg}$  (where we measure the standard deviation from a sample of 20 particles). The defect particle has a mass of 81.6 mg, which corresponds to 58.68% of the normal particle mass.

We excite the defect particle using an external magnetic field that we generate using a conductive wire that we place over the particle at a height of 3 mm. We generate the AC current that flows through the wire from a Lock-In amplifier (SR860 500 kHz DSP Lock-in Amplifier), and we amplify it with an audio amplifier (Topping TP22, class D). The equation that describes the force that the wire exerts on a magnet a distance  $r$  from it is

$$F_{\text{wire}}(r) = \frac{I\mu_0\mathcal{M}}{2\pi} \frac{h^2 - r^2}{(h^2 + r^2)^2}, \quad (1)$$

where  $h$  is the height of the wire from the plane of floating discs,  $I$  is the wire current,  $\mu_0 = 4\pi \cdot 10^{-7} \text{ N A}^{-2}$  is the magnetic permeability, and  $\mathcal{M} = 7.8 \cdot 10^{-3} \text{ Am}^2$  is the magnetic moment of the floating disc. See the appendix for the derivation of Eq. (1). We use harmonic excitations in our experiment, so the current through the wire is  $I(t) = aI_0 \sin(2\pi ft)$ , where  $f$  is the drive frequency (in Hz),  $a$  is the drive-voltage amplitude (in Volts), and  $I_0 = 0.1 \text{ A V}^{-1}$  is the current per unit voltage that we measure in the wire.

The magnets repel each other. In the ideal situation of a perfect dipole–dipole interaction, the magnetic force between two repelling magnets is

$$F_{\text{magnet}}(r) = Ar^p, \quad (2)$$

where  $r$  is the distance (in meters) between the two center points of the magnets,  $p = -4$ , and  $A = 3\mu_0\mathcal{M}^2/2\pi$ . Although Eq. (2) is reasonable for large separation distances, we obtain better agreement by empirically determining  $A$  and  $p$ . Because

the force between two magnetic dipoles is too small to measure directly, we create a pair of plastic plates, with 25 magnets attached to each plate. We position the plates to align each pair of cylindrical magnets from opposite plates through their radial directions. We measure the repulsive force as a function of the displacement between these two plates in a materials tester (Instron ElectroPuls E3000). The distance between the magnets on each plate is large enough (specifically, it is 2.5 cm) so that we can neglect interactions between magnets that are not aligned. The distance between a magnet on the first plate and the non-aligned magnets on the other plate is larger than 25 mm. As one can see in Fig. 1(c), the interaction force already tends to 0 for distances that are significantly smaller than 25 mm. Consequently, the measured force is approximately equal to the sum of the repulsive force of the 25 isolated magnet pairs. We fit the data using Eq. (2), which yields  $p \approx -4.2$  and  $A \approx 3.8 \cdot 10^{-12} \text{ N/m}^p$  [see Fig. 1(c)].

We monitor the motion of the central particle using a laser vibrometer (Polytec CLV-2534), and we record the dynamics of the rest of the lattice using a digital camera (Point Grey GS3-U3-41C6C-C) with a frame rate of 90 fps. We analyze the images using digital-image-correlation (DIC) software (VIC-2D) to determine each particle's velocity. We inspect half of the lattice, as the cables that are connected to the driving wire block most of the system's other half [see Fig. 1(a)]. Due to imperfections at the bottom of the glass disks (e.g., dust, scratches, and so on) and the fact that mass is not distributed evenly on a disk, a few particles start to rotate when they are levitated by the air that flows out of the air-bearing table. The image-correlation software then loses track of them. We ignore these rotating disks in our subsequent analysis. To estimate the value of the damping coefficient  $\gamma$  of a linear dashpot term, we excite the center particle in the experiment and let the resulting temporal amplitude decay to rest once we switch off the excitation. We then perform a linear regression on the logarithm of the temporal data to obtain an estimate for the decay rate  $\beta$ , where we are assuming an exponential decay that is proportional to  $e^{\beta t}$ . We then choose  $\gamma$  by minimizing the objective function  $|\beta - \beta_r(\gamma)|$ , where  $\beta_r(\gamma)$  is the real part of the eigenvalue that is associated with the defect mode of the linear system with damping but no driving. (See Eq. (13) with  $a = 0$ .) We do this because the linear defect mode in the damped, undriven system decays exponentially to 0 with a rate of  $\beta_r(\gamma)$ . We give details of the linear problem in Sec. III B. This procedure yields  $\gamma \approx 10.52 \cdot 10^{-3} \text{ N s/m}$ . The lattice particles are always in motion with at least small speeds, even in the absence of excitation. This is due to interactions with the air flow from the table and imperfections (e.g., nonaxisymmetric mass distributions) of the particles. We use this motion to estimate the noise in the system. To evaluate the amount of noise, we record the lattice motion without excitation as a comparison; see the appendix for details about the noise estimation. We summarize the values of all parameters in Table I.

TABLE I: Summary of the parameter values in our experimental setup.

Description	Symbol	Value (measured)	Description	Symbol	Value (fitted)
Mass of bulk magnet	$M_b$	138.2 mg	Magnetic coefficient	$A$	$3.8 \cdot 10^{-12} \text{ N/m}^p$
Defect mass	$M_\delta$	81.6 mg	Nonlinearity	$p$	-4.2
Static-equilibrium distance	$\delta$	13.7 mm	Damping coefficient	$\gamma$	$10.52 \cdot 10^{-3} \text{ N s/m}$
Wire height	$h$	3 mm	Magnetic moment	$\mathcal{M}$	$7.8 \cdot 10^{-3} \text{ A m}^2$

### III. THEORETICAL SETUP

#### A. Model Equations

Our goal is to study NLMs in a 2D hexagonal lattice. In selecting equations to model the system that we described in Sec. II, we seek the simplest possible model that incorporates the ingredients (nonlinearity, discreteness, and appropriate dimensionality) that are essential for NLMs and also yield reasonable agreement with experimental data. It is in this spirit that we develop our model equations. After doing so, we briefly discuss model simplifications.

We consider a hexagonally packed lattice of magnets. We use the lattice basis vectors  $\mathbf{e}_1 = (1, 0)$  and  $\mathbf{e}_2 = (1/2, \sqrt{3}/2)$ . Let  $\mathbf{q}_{m,n}(t) = (x_{m,n}(t), y_{m,n}(t)) \in \mathbb{R}^2$  denote the displacement from the static equilibrium of the magnet at position  $\mathbf{p} = \delta(m\mathbf{e}_1 + n\mathbf{e}_2)$  in the plane [see Fig. 2(a)], where  $\delta$  is the center-to-center distance between two particles at static equilibrium. The lattice indices  $m$  and  $n$  take the values  $m, n \in \{-w, -(w-1), \dots, 0, \dots, w-1, w\}$ , where  $w$  is the number of magnets along an edge of the hexagon. The lattice boundary is given by the hexagon with magnets at positions  $(w\delta \cos(j\pi/3), w\delta \sin(j\pi/3))$ , where  $j \in \{0, 1, \dots, w-1\}$  [see Fig. 2(b)]. For our fixed boundary conditions along the edge of the hexagonal boundary,  $\mathbf{q}_{m,n}(t) = 0$  if  $|m+n| > w$ .

One can express the distance between the magnet with index  $(m, n)$  and one of its nearest neighbors in terms of the displacements  $x_{m,n}$  and  $y_{m,n}$  of the magnets from their respective static-equilibrium positions. Once we determine this distance, we

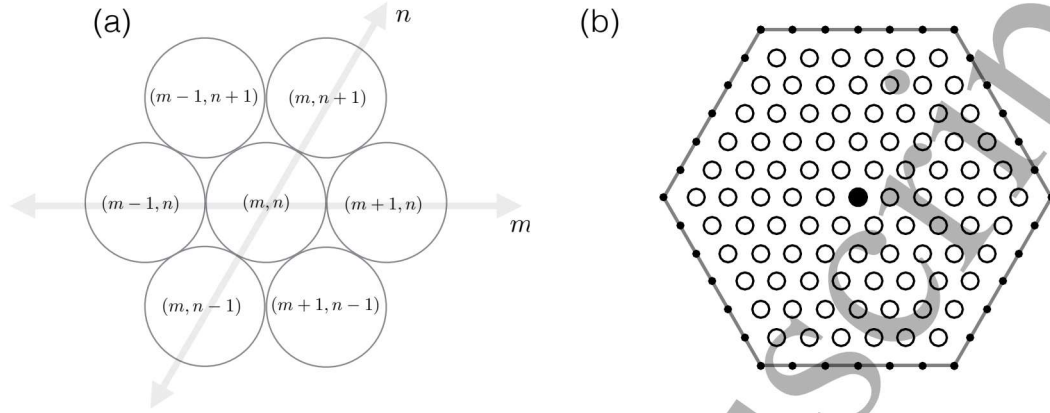


FIG. 2: (a) Orientation for our convention of indexing particles in a hexagonal lattice. The  $m$  axis and  $n$  axis meet at an angle of  $\theta = \pi/3$ . (b) A hexagonal lattice with  $w = 6$  magnets along each edge of the lattice. The empty circles and solid center circle represent the locations of the magnets in static equilibrium. The outer hexagonal boundary is the solid gray hexagon that encloses the lattice. On the boundary, the solid points represent fixed (i.e., immovable) magnets. There are  $w + 1$  such magnets along each edge of the boundary. The solid circle represents the defect particle, which has index  $(m, n) = (0, 0)$ .

compute the resulting force using Eq. (2). Summing the forces from each of the six nearest neighbors and applying Newton's second law leads to the following equations of motion:

$$M_{m,n} \ddot{\mathbf{q}}_{m,n} = -\mathbf{F}_0(\mathbf{q}_{m+1,n} - \mathbf{q}_{m,n}) - \mathbf{F}_1(\mathbf{q}_{m,n+1} - \mathbf{q}_{m,n}) + \mathbf{F}_{-1}(\mathbf{q}_{m,n} - \mathbf{q}_{m-1,n+1}) \\ + \mathbf{F}_0(\mathbf{q}_{m,n} - \mathbf{q}_{m-1,n}) + \mathbf{F}_1(\mathbf{q}_{m,n} - \mathbf{q}_{m,n-1}) - \mathbf{F}_{-1}(\mathbf{q}_{m+1,n-1} - \mathbf{q}_{m,n}) - \gamma \dot{\mathbf{q}}_{m,n} + \mathbf{F}_{m,n}^{\text{ext}}(t). \quad (3)$$

The vector functions  $\mathbf{F}_j(\mathbf{q}) = \mathbf{F}_j(x, y) \in \mathbb{R}^2$  have a magnitude of

$$|\mathbf{F}_j(x, y)| = A \left[ \sqrt{(\delta \cos(\theta_j) + x)^2 + (\delta \sin(\theta_j) + y)^2} \right]^p, \quad \theta_j = \frac{j\pi}{3}, \quad j \in \{-1, 0, 1\}.$$

The mass of the magnet with index  $(m, n)$  is  $M_{m,n}$ . The dashpot term  $\gamma \dot{\mathbf{q}}_{m,n}$  is a phenomenological term that we add to account for damping. Using such a term has yielded reasonable agreement with experiments in other, similar lattices [19, 37, 38]. The quantity  $\mathbf{F}_{m,n}^{\text{ext}}$  is the external force that we apply to the magnet at  $(m, n)$ . In the present article, we consider excitations via a wire that is directly above the center of the lattice. The magnitude of the excitation is given by Eq. (1). Therefore,

$$\mathbf{F}_{0,0}^{\text{ext}}(t) = a \sin(2\pi ft) \frac{I_0 \mu_0 \mathcal{M}}{2\pi} \begin{pmatrix} \cos(\phi) \frac{h^2 - x_{0,0}^2}{(h^2 + x_{0,0}^2)^2} \\ \sin(\phi) \frac{h^2 - y_{0,0}^2}{(h^2 + y_{0,0}^2)^2} \end{pmatrix}, \quad (4)$$

where  $\phi$  is the angle of the excitation and  $\mathbf{F}_{m,n}^{\text{ext}} = 0$  when  $m \neq 0$  and  $n \neq 0$ . In our experiments and in most of our numerical computations, the excitation angle is  $\phi = \pi/2$ , so we excite only the  $y$ -component of the center magnet. We will also explore some other excitation angles. As we discuss in the appendix, the lattice forces dominate the dynamics. The wire has only a small effect on magnets other than the one in the center of the lattice. For example, at static equilibrium, the force that is exerted on the center magnet by the wire is two orders of magnitude larger than the force that the wire exerts on the center magnet's nearest neighbors. Compare the results from inserting  $r = 0$  and  $r = \delta$  into Eq. (1).

In our model, we ignore effects beyond nearest-neighbor coupling of the magnetic interactions. It is known that such long-range effects can alter the structure of localized modes. For example, it was shown in [39] that the spatial decay of breathers can transition from exponential spatial decay to algebraic decay in lattices with algebraically decaying interaction forces (as is the case in our model) for lattices with sufficiently many sites. More recently, Molerón et al. [38] studied NLMs in a 1D magnetic lattice using a model with long-range interactions. Although the differences between long-range and nearest-neighbor lattices that were considered in [38] are detectable, they are still small. For example, at static equilibrium, the force that is exerted on the center magnet by its nearest neighbors is one order of magnitude larger than that exerted by its next-nearest neighbor. (Compare the results from inserting  $r = \delta$  and  $r = 2\delta$  into Eq. (2).) Therefore, to keep our model as simple as possible, we ignore such small long-range effects.

In our analysis of experimental data, we ignore magnets that are rotating, so our model does not account for rotation. This leaves air resistance as the primary source of damping. Given the size of the magnets and velocities that we consider, we employ

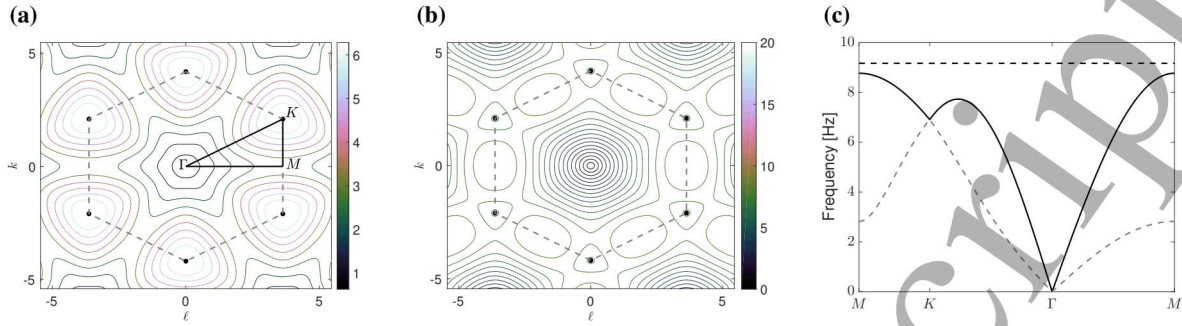


FIG. 3: (Color Online) **(a)** Contour plot of the bottom dispersion surface. We show the irreducible Brillouin zone as the triangle with magnets at the points that we mark by  $M$ ,  $K$ , and  $\Gamma$ . **(b)** Contour plot of top dispersion surface. **(c)** Band structure along the edge of the irreducible Brillouin zone [also see the triangle in panel (a)] for the bottom (dashed gray curve) and top (solid black curve) dispersion surfaces. The horizontal dashed curve corresponds to the defect-mode frequency  $f \approx 9.17$  Hz in a finite-dimensional system with a mass ratio of  $M_\delta/M_b \approx 0.5868$ , where  $M_\delta$  denotes the mass of the defect magnet and  $M_b$  denotes the mass of the other (“bulk”) magnets.

a linear dashpot [40]. We also assume that the magnets stay in a plane. We validate the many assumptions that we made in formulating the model in Eq. (3) via a direct comparison with experimental results in Sec. IV.

For the remainder of the manuscript, we fix all parameters of the model (and we summarize them in Table I), except for the excitation amplitude  $a$ , frequency  $f$ , and angle  $\phi$ . We will specify these in our various examples. In all cases, we examine a lattice with a single defect particle in the center and a hexagonal boundary with a length of  $w = 6$  magnets (see Fig. 2). Importantly, we do not fit the parameter values to the reported experimental results. Instead, we determine them beforehand using the procedures that we detailed in Sec. II.

## B. Linear Analysis

We start with the basic linear theory of localized modes for our hexagonal magnetic lattice. We are particularly interested in modes with frequencies that lie above the cutoff frequency of the pass band. We first derive an analytical expression for the cutoff frequency, which is straightforward for an infinite-dimensional Hamiltonian system (i.e., with all integers  $m$  and  $n$ , along with  $a = 0$  and  $\gamma = 0$ ). We then numerically estimate the frequency of a linear mode that is associated with the defect in the finite-dimensional Hamiltonian system. Finally, we compute linear localized modes in the associated finite-dimensional damped, driven system.

Assuming small strains, such that

$$\frac{|\mathbf{q}_{m\pm 1,n} - \mathbf{q}_{m,n}|}{\delta} \ll 1, \quad \frac{|\mathbf{q}_{m,n\pm 1} - \mathbf{q}_{m,n}|}{\delta} \ll 1, \quad \frac{|\mathbf{q}_{m\pm 1,n\mp 1} - \mathbf{q}_{m,n}|}{\delta} \ll 1, \quad (5)$$

one can Taylor expand to obtain

$$\mathbf{F}_j(\mathbf{q}) \approx \mathbf{F}_j(\mathbf{q}_0) + D\mathbf{F}_j(\mathbf{q}_0)\mathbf{q},$$

where  $D\mathbf{F}_j$  is the Jacobian matrix of  $\mathbf{F}_j$ . Using this notation, the linearized equations of motion are

$$\begin{aligned} M_{m,n}\ddot{\mathbf{q}}_{m,n} = & -D\mathbf{F}_0(\mathbf{q}_{m+1,n} + \mathbf{q}_{m-1,n}) - D\mathbf{F}_1(\mathbf{q}_{m,n+1} + \mathbf{q}_{m,n-1}) \\ & - D\mathbf{F}_{-1}(\mathbf{q}_{m-1,n+1} + \mathbf{q}_{m+1,n-1}) + 2(D\mathbf{F}_0 + D\mathbf{F}_1 + D\mathbf{F}_{-1})\mathbf{q}_{m,n}, \end{aligned} \quad (6)$$

where

$$D\mathbf{F}_j = \begin{pmatrix} a_j & b_j \\ c_j & d_j \end{pmatrix}, \quad j \in \{-1, 0, 1\},$$

with

$$\begin{aligned} a_{-1} &= p\hat{\delta}, & b_{-1} &= 0, & c_{-1} &= 0, & d_{-1} &= \hat{\delta}, \\ a_0 &= \frac{3+p}{4}\hat{\delta}, & b_0 &= \frac{\sqrt{3}(p-1)}{4}\hat{\delta}, & c_0 &= b_0, & d_0 &= \frac{1+3p}{4}\hat{\delta}, \\ a_1 &= a_0, & b_1 &= -b_0, & c_1 &= -c_0, & d_1 &= d_0, \end{aligned}$$

where  $\hat{\delta} \equiv A\delta^{p-1}$ . For a monoatomic system (in which all magnets are identical, such that  $M_{m,n} = M_b$ ), the linear system has plane-wave solutions

$$\mathbf{q}_{m,n} = \mathbf{q}_0 \exp\left(i(km + \frac{n}{2}(k + \sqrt{3}\ell))\right) e^{i\omega t}, \quad \mathbf{q}_0 \in \mathbb{C}^2, \quad k, \ell, \omega \in \mathbb{R},$$

where the wavenumbers  $k, \ell$  and angular frequency  $\omega = \omega(k, \ell)$  satisfy the dispersion relationship

$$[\omega(k, \ell)]^2 = \frac{\omega_a + \omega_d \pm \sqrt{(\omega_a + \omega_d)^2 - 4(\omega_a\omega_d - \omega_b\omega_c)}}{2}, \quad (7)$$

with

$$\omega_\alpha(k, \ell) = (-2\alpha_{-1} \cos(k) - 2\alpha_0 \cos(k/2 + \sqrt{3}/2\ell) - 2\alpha_1 \cos(k/2 - \sqrt{3}/2\ell) + 2(\alpha_{-1} + \alpha_0 + \alpha_1))/M_b$$

and coefficients  $\alpha_j \in \{a_j, b_j, c_j, d_j\}$  (with  $j \in \{-1, 0, 1\}$ ). In Fig. 3(a,b), we show contour plots of the two dispersion surfaces from Eq. (7). In Fig. 3(c), we show the dispersion curves along the edge of the irreducible Brillouin zone. The cutoff value of the pass band has the wavenumber pair  $(k, \ell) = (0, 2\pi/3)$ , which is where the dispersion curve attains its maximum value. For the parameter values in Table I, the cutoff frequency is  $f_c = \omega(0, 2\pi/3)/(2\pi) \approx 8.77$  Hz, where  $\omega_+$  corresponds to the top dispersion surface.

The presence of the lighter defect introduces a linear mode into the system that is localized in space and oscillates with a frequency above the cutoff frequency of the linear monoatomic system. With the light-mass defect at the center of the lattice, we write

$$M_{m,n} = \begin{cases} M_\delta, & n = 0 \text{ and } m = 0 \\ M_b, & \text{otherwise,} \end{cases} \quad (8)$$

where  $(0, 0)$  is the index of the mass defect with mass  $M_\delta$ , the quantity  $M_b$  is the mass of a magnet in the “bulk” (i.e., the non-defect mass), and  $M_\delta < M_b$ . We numerically compute the linear modes of the system with a mass defect, and we are thereby able to consider finite lattices. We use a hexagonal boundary with an edge length of  $w = 6$  magnets [see Fig. 2(b)]. One can embed this lattice into a square matrix of size  $N \times N$ , where  $N = 2w - 1$  is the number magnets along the  $n = 0$  line of the lattice. Let  $X(t)$  be the  $N \times N$  matrix whose  $(m, n)$ th entry is  $x_{m,n}(t)$ , and let  $Y(t)$  be the  $N \times N$  matrix whose  $(m, n)$ th entry is  $y_{m,n}(t)$ . We enforce the fixed hexagonal boundaries by setting the displacements of magnets with indices  $(m, n)$  such that  $|m + n| > w$  to 0. We define the  $N \times N$  matrix operators  $L_\alpha$  through

$$L_\alpha Y = \alpha_1 DY + \alpha_0 YD + \alpha_{-1}(E^T Y E^T + E Y E - 2Y), \quad (9)$$

where  $\alpha_j \in \{a_j, b_j, c_j, d_j\}$  (with  $j \in \{-1, 0, 1\}$ ); the  $N \times N$  tridiagonal matrix  $D$  has 1 entries on the super-diagonals and sub-diagonals, 2 entries along the diagonal, and 0 entries everywhere else;  $E$  is an  $N \times N$  matrix with 1 entries along the super-diagonal and 0 entries everywhere else; and  $E^T$  is the transpose of  $E$ . With these definitions, Eq. (6) becomes

$$\begin{aligned} M \circ \ddot{X}(t) &= L_a X(t) + L_b Y(t), \\ M \circ \ddot{Y}(t) &= L_c X(t) + L_d Y(t), \end{aligned} \quad (10)$$

where  $M$  is an  $N \times N$  matrix in which all entries except the  $(0, 0)$ th entry (which is equal to  $M_\delta$ ) are equal to  $M_b$ . The operation  $\circ$  denotes pointwise multiplication (i.e., the Hadamard product). The system (10) has solutions of the form  $X(t) = \tilde{X}e^{i\omega t}$  and  $Y(t) = \tilde{Y}e^{i\omega t}$ , where  $\tilde{X}$  and  $\tilde{Y}$  are  $N \times N$  time-independent matrices and

$$-\omega^2 \begin{pmatrix} M \circ \tilde{X} \\ M \circ \tilde{Y} \end{pmatrix} = \begin{pmatrix} L_a & L_b \\ L_c & L_d \end{pmatrix} \begin{pmatrix} \tilde{X} \\ \tilde{Y} \end{pmatrix}. \quad (11)$$

One can cast Eq. (11) as a standard eigenvalue problem by letting  $\lambda = -\omega^2$  and unwrapping the  $\tilde{X}$  and  $\tilde{Y}$  matrices into equivalent row vectors and reshaping the block matrix (with entries given by  $L_\alpha$ ) into a corresponding  $2N^2 \times 2N^2$  matrix. One can then numerically solve the resulting eigenvalue problem to obtain  $2N^2$  eigenvalues and their corresponding modes. Using the values in Table I and  $w = 6$  (which yields  $N = 11$ ), we see that two eigenvalues (each with a frequency of  $\sqrt{-\lambda}/(2\pi) = \omega/(2\pi) = f_d \approx 9.17$ ) lie above the cutoff frequency  $f_c \approx 8.77$  Hz. The rotational symmetry of order 6 of the hexagonal lattice suggests that eigenvalues come in nearly resonant triplets, rather than in pairs [41]. Although this is indeed true for a homogeneous hexagonal lattice, the presence of the defect splits the largest nearly resonant triplet into a pair of eigenvalues with a frequency above the cutoff (representing the defect frequency) and a single, non-repeated eigenvalue. The spatial structure corresponding to the three largest eigenvalues confirms that there are only two defect modes. In particular, the spatial structure of the modes that correspond to the frequency  $f_d$  is localized [see Fig. 4(a,b)]. The spatial structure of the mode that corresponds to the next-largest eigenvalue is spatially extended [see Fig. 4(c)].

Now suppose that there is driving and damping. Near the  $(X(t), Y(t)) \equiv 0$  background state, equations (10) yield the following approximate system:

$$M \circ \ddot{X}(t) = L_a X(t) + L_b Y(t) - \gamma \dot{X}(t) + a \mathcal{A} \cos(\phi) \sin(2\pi f t), \quad (12)$$

$$M \circ \ddot{Y}(t) = L_c X(t) + L_d Y(t) - \gamma \dot{Y}(t) + a \mathcal{A} \sin(\phi) \sin(2\pi f t), \quad (13)$$

where  $\mathcal{A}$  is an  $N \times N$  matrix that has all 0 entries except for the single nonzero entry

$$\mathcal{A}_{0,0} = \frac{I_0 \mu_0 \mathcal{M}}{2\pi h^2}.$$

We obtain  $\mathcal{A}$  by expanding the external drive function  $\mathbf{F}^{\text{ext}}$  near the vanishing displacements and maintaining the leading, non-vanishing term. We can then find solutions of the system (12,13) in the form

$$X(t) = \tilde{X}_1 \cos(2\pi f t) + \tilde{X}_2 \sin(2\pi f t), \quad Y(t) = \tilde{Y}_1 \cos(2\pi f t) + \tilde{Y}_2 \sin(2\pi f t), \quad (14)$$

where we obtain the  $N \times N$  matrices  $\tilde{X}_1$ ,  $\tilde{X}_2$ ,  $\tilde{Y}_1$ , and  $\tilde{Y}_2$  by substituting Eq. (14) into Eqs. (12) and (13) and then solving the resulting system of linear equations.

We use root mean square (RMS) quantities as our principal diagnostic for evaluating our results, such as in our numerical continuations. Most commonly, we compute the RMS of the velocity of the  $y$ -component of the center particle (i.e.,  $\dot{y}_{0,0}$ ). In this case,

$$\text{RMS} = \sqrt{\frac{\int_0^T \dot{y}_{0,0}^2(t) dt}{T}},$$

where  $T = 1/f$  is the period of the excitation frequency. We show a plot of the RMS of the linear state (14) in Fig. 4(d) as a function of the excitation frequency for a fixed amplitude of  $a = 0.01$  mV and an excitation angle of  $\phi = \pi/2$ . The lone resonant peak above the cutoff point is close to the estimated defect frequency  $f_d \approx 9.17$  Hz.

In Fig. 4(e), we show a frequency sweep in our experiment for  $a = 4$  mV and  $\phi = \pi/2$ . We show the theoretical values of the cutoff frequency  $f_c \approx 8.77$  Hz and defect frequency  $f_d \approx 9.17$  Hz that we found in Sec. III B as vertical solid and dashed lines, respectively. We see that the experimental resonant peak is close to the theoretical value. To obtain a cleaner resonant peak, we use an excitation amplitude that is large enough to overcome the noise of the system. One such amplitude is  $a = 4$  mV. As we will see in Sec. IV, an excitation amplitude of  $a = 4$  mV is already in the nonlinear regime of the system.

### C. Numerical Methods for the Computation of Nonlinear Localized Modes and Their Stability

For the remainder of our paper, we focus on how the presence of nonlinearity affects the “defect-induced” linear localized modes of the system [see, e.g., Fig. 4(d)]. We refer to these solutions, which are localized in space and periodic in time, as nonlinear localized modes (NLMs). We compute them numerically in the following manner. We compute time-periodic orbits of Eq. (3) with period  $T = 1/f$  to high precision by finding roots of the map  $G = \mathbf{x}(T) - \mathbf{x}(0)$ , where  $\mathbf{x}(T)$  is the solution of Eq. (3) at time  $T$  with initial condition  $\mathbf{x}(0)$  and  $\mathbf{x} \in \mathbb{R}^{4N^2}$  is the vector that results from reshaping the matrix with elements  $x_{m,n}$ ,  $y_{m,n}$ ,  $\dot{x}_{m,n}$ , and  $\dot{y}_{m,n}$  into row vectors and concatenating them into a single vector. We obtain roots of the map  $G$  using a Jacobian-free Newton–Krylov method [42] with an initial guess of our linear state (14). We perform numerical continuations using a pseudo-arclength algorithm [43] with the excitation frequency  $f$  or amplitude  $a$  as our continuation parameter. We determine the linear stability of each solution  $\mathbf{x}$  by solving the variational equations  $V' = DG \cdot V$  with the initial condition  $V(0) = I$ , where  $I$  denotes the identity matrix and  $DG$  is the  $4N^2 \times 4N^2$  Jacobian matrix of the right-hand side of Eq. (3).

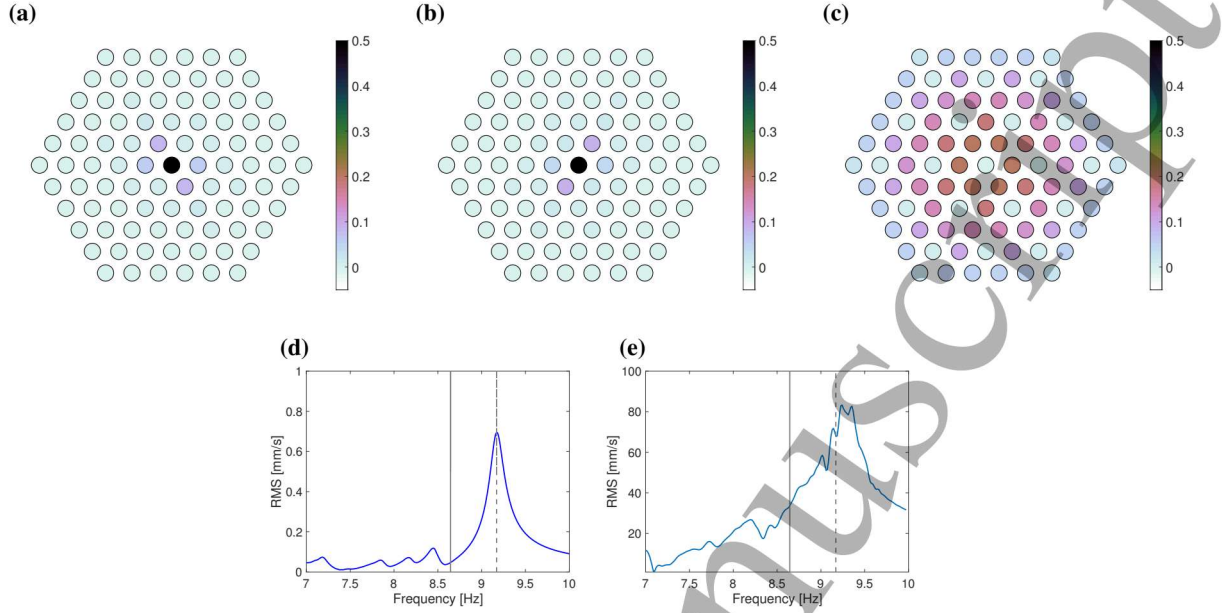


FIG. 4: **(a,b)** Shapes of the two modes with defect frequency  $f_d \approx 9.17$  Hz of the linear Hamiltonian system (6) with  $w = 6$  magnets along each edge of the boundary. The color intensity at each point  $(m, n)$  corresponds to  $\sqrt{x_{m,n}^2 + y_{m,n}^2}$ . **(c)** Shape of the mode that corresponds to the cutoff frequency  $f_c \approx 8.77$  Hz for the same system as in (a,b). **(d)** Root mean square (RMS) of  $\dot{y}_{0,0}$  of the linear damped, driven solution (14) as a function of the drive frequency  $f$  with excitation amplitude  $a = 0.01$  mV and  $\phi = \pi/2$ . **(e)** RMS of the velocity of the center particle of the experimental frequency sweep with  $a = 4$  mV and  $\phi = \pi/2$ .

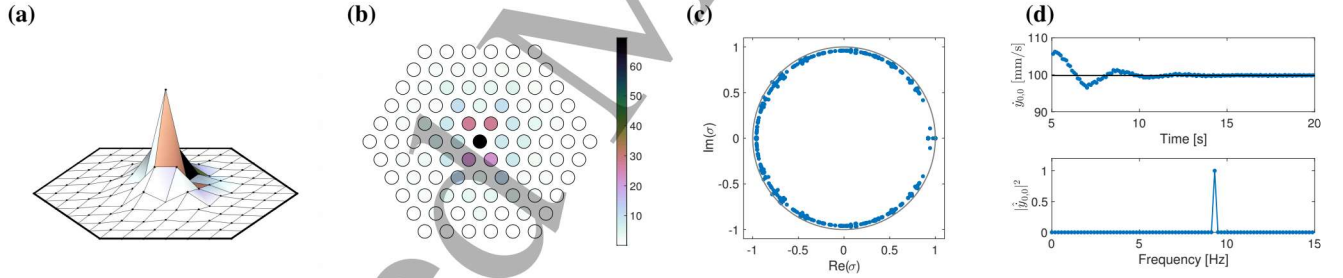


FIG. 5: Nonlinear localized mode of Eq. (3) that we obtain using a Newton–Krylov method for  $a = 4$  mV,  $\phi = \pi/2$ , and  $f = 9.3$  Hz. **(a)** A surface plot of the NLM. We show the RMS velocity of each magnet in the lattice. **(b)** Intensity plot of the NLM, where the color intensity corresponds to the RMS. **(c)** Floquet multipliers  $\sigma$  (blue markers) that are associated with the NLM in the complex plane. We show the unit circle in gray. All multipliers lie within or on the unit circle, indicating that this solution is stable. **(d)** In the top panel, we show local maxima of the time series of  $\dot{y}_{0,0}$  when evolving zero initial data (i.e., the initial values of all variables are equal to 0) for  $a = 4$  mV,  $\phi = \pi/2$ , and  $f = 9.3$  Hz. We approach the value  $\dot{y}_{0,0} \approx 99.8$  mm/s of the stable NLM. (See the black line.) In the bottom panel, we show the Fourier transform of the final 5 seconds of the time series of  $\dot{y}_{0,0}$ . This reveals a single large peak at frequency  $f \approx 9.3$  Hz.

evaluated at the solution  $\mathbf{x}$  [44]. We calculate the Floquet multipliers, which we denote hereafter by  $\sigma$ , for a solution by computing the eigenvalues of the matrix  $V(T)$ . If all of the Floquet multipliers of a solution have an absolute value that is less than or equal to 1, we say that the solution is “linearly stable”. Otherwise, we say that the solution is “unstable”. The Floquet multipliers only give information about the spectral stability of the solutions, and marginal instabilities that are associated with unit Floquet multipliers and nonlinear instabilities are possible. Therefore, we verify stability through numerical simulations. In our continuation diagrams, solid blue segments correspond to stable parameter regions and dashed red segments correspond to unstable regions. We compute the Floquet multipliers after we obtain a solution with the Newton–Krylov method to avoid repeatedly solving the large variational system. Such a computation would be necessary if we were using a standard Newton method, because the Jacobian of the map  $G$  is  $V(T) - I$ .

## IV. MAIN RESULTS

### A. Numerical NLMs

Using the Newton–Krylov method that we described in Sec. III C, we obtain a time-periodic solution with  $f = 9.3$  Hz,  $a = 4$  mV, and  $\phi = \pi/2$ . Additionally, because  $f = 9.3 > 8.77 \approx f_c$ , this solution is localized in space [see Fig. 5(a)]. The dominant peak is at the center of the lattice, the magnets that are adjacent to the center magnet at angles  $\pi/3$ ,  $2\pi/3$ ,  $4\pi/3$ , and  $5\pi/3$  have the next-largest amplitudes [see Fig. 5(b)]. This is not surprising, because we are exciting the lattice along the  $\phi = \pi/2$  direction. The Floquet multipliers that are associated with this solution each have a magnitude that is no more than 1, indicating that the solution is stable [see Fig. 5(c)]. Indeed, upon simulating Eq. (3) with the initial values of all variables equal to 0 (i.e., “zero initial data”) and  $f = 9.3$  Hz,  $a = 4$  mV, and  $\phi = \pi/2$ , the dynamics approaches this stable NLM. [See the top panel of Fig. 5(d).] As expected, the Fourier transform of the corresponding time series is localized around the frequency  $f \approx 9.3$  Hz.

The spatial decay of the tails of the NLM depends on which direction of observation one considers. For example, if one measures the RMS velocity of the magnets that lie along the  $\theta = \pi/3$  direction, the decay appears to be exponential or faster. See the solid blue squares in Fig. 6(a), which shows the RMS velocity versus distance from the origin (following the  $\theta = \pi/3$  direction) in a semilogarithmic plot for the NLM from Fig. 5 [i.e., for the NLM with  $f = 9.3$  Hz,  $a = 4$  mV, and  $\phi = \pi/2$ ]. This is consistent with the spatial decay properties of breathers in continuous-space settings, such as the ones in the quintic Ginzburg–Landau equation that were studied in [45]. The tails of the breathers in [45] decay at rate  $e^{-br}/\sqrt{r}$ , where  $b > 0$  is a constant. The solid yellow circles in Fig. 6(a) illustrate a similar decay for the magnets along the  $\theta = 0$  direction for our NLM solution, although we observe some modulation in the decay profile, in contrast to the dynamics when  $\theta = \pi/3$ . (Modulations in spatial decay have been studied in other settings, such as in the biharmonic  $\phi^4$  model [46].) We observe similar decay properties for an NLM with  $f = 9.3$  Hz,  $a = 5.5$  mV and  $\phi = \pi/2$  [see Fig. 6(b)].

### B. Experimental NLMs

In our experiments, it is difficult to initialize the system with predetermined positions and velocities. To obtain an NLM, we excite the system with a small amplitude ( $a = 1$  mV) which we increase gradually to the value  $a = 4$  mV over about 3 minutes. Because we predict that there is a stable NLM at the resulting parameter values, we record data for sufficiently long (specifically, after 90 periods of motion have elapsed) once we attain the value  $a = 4$  mV. We track the velocities at the center particle with a laser vibrometer (see Sec. II), and we record the time series of the magnet velocities using an oscilloscope. [See the top panel of Fig. 6(c).] As expected, we obtain dynamics that are periodic in time, as we can see not only with the time series but also via its Fourier transform [which we show in the bottom panel of Fig. 6(c)]. We obtain similar experimental results for an amplitude of  $a = 5.5$  mV.

To examine the spatial decay of the experimental NLM, we record the positions of the magnets in half of the lattice using a digital camera (see Sec. II). By numerically differentiating the positions, we obtain an estimate for the velocities of these magnets. We were unable to do a complete full-field realization, because the DIC loses track of some magnets (if, e.g., the magnets begin to spin). However, we captured enough data to compute the decay along the two primary directions ( $\theta = \pi/3$  and  $\theta = 0$ ) that we examined in our numerical NLMs. For data that we obtained with  $f = 9.3$  Hz,  $a = 4$  mV, and  $\phi = \pi/2$ , the open blue squares in Fig. 6(a) show the decay along the  $\theta = \pi/3$  direction and the open yellow circles show the decay along the  $\theta = 0$  direction. The horizontal dashed line is our estimated mean value of the noise (see Sec. II). We show the experimental decay rates along with our numerical results. Although the numerical values overestimate the RMS velocity, the agreement is still reasonable, especially for the center magnet. We find similar decay properties in our experiment with  $f = 9.3$  Hz,  $a = 5.5$  mV, and  $\phi = \pi/2$ . [See the open markers of Fig. 6(b).]

Recall that we do not tune the numerical results to fit the experimentally obtained NLM solution. Instead, we determine each of the parameter values beforehand, as described in Sec. II.

### C. Frequency Continuation

In Figs. 4(e) and 6(a,b), we demonstrate that our model (3) agrees reasonably well with our experimental data. We now conduct a series of numerical computations in the form of parameter continuation (see Sec. III C for a description of our procedure) to get a better sense of the role of the nonlinearity in Eq. (3) and its interplay with the disorder (at the central magnet) and the discreteness of the model. We return to our experiments in Sec. IV D to see what nonlinear effects we are able to capture in the laboratory.

We first perform continuation with respect to the excitation frequency  $f$  for a fixed excitation angle  $\phi = \pi/2$  for various values of the excitation amplitude  $a$ . We thereby generate nonlinear analogs of the linear resonant peak that we showed in Fig. 4(d). In Fig. 7(a), we show frequency continuations for our two drive amplitudes,  $a = 4$  mV and  $a = 5.5$ , of the NLMs from Fig. 5 and

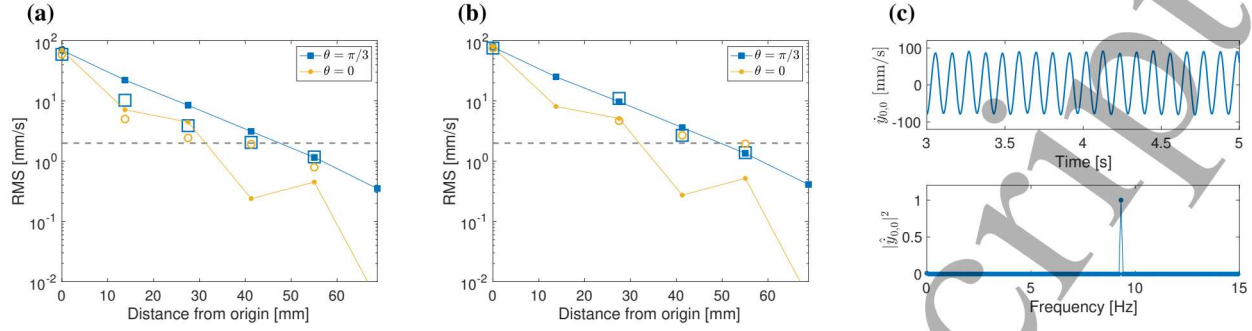


FIG. 6: **(a)** Decay of the NLM in the  $\theta = \pi/3$  (blue squares) and  $\theta = 0$  (yellow circles) directions for a drive amplitude of  $a = 4$  mV, drive angle of  $\phi = \pi/2$ , and drive frequency of  $f = 9.3$  Hz. We show the RMS velocity versus the distance to the origin of the lattice. We show experimental results as open markers and the numerical results as solid markers that are connected by lines. The dashed horizontal line is an estimation of the noise floor of the system (see the appendix). **(b)** The same as panel (a), but for a drive amplitude of  $a = 5.5$  mV. **(c)** Time series (top panel) of the center particle of the experimental NLM and the corresponding Fourier transform (bottom panel) with  $\phi = \pi/2$ ,  $f = 9.3$  Hz, and  $a = 4$  mV. Despite the presence of some noise, the solution is predominantly periodic in time. Indeed, the Fourier transform of the time signal is highly localized around the frequency  $f = 9.3$  Hz.

Figs. 6(a,b). From comparing these frequency continuations to the linear case in Fig. 4(d), we see that the nonlinearity deforms the peak, which becomes narrower and starts to bend towards higher frequencies. The nonlinearity also destabilizes the solutions at some critical frequency; this occurs at  $f \approx 9.29$  Hz for  $a = 4$  mV and at  $f \approx 9.31$  Hz for  $a = 5.5$  mV. Therefore, the NLM in Fig. 6(c) is unstable. Our numerical computations predicted this NLM to be unstable, so it is notable that we are able to access it in our experiments. Although this seems to imply that our theory is inconsistent with our experiments for the parameter values  $f \approx 9.31$  Hz and  $a = 5.5$  mV, the instability of the NLM for these parameter values is rather weak (with  $\max(|\sigma_i|) \approx 1.007$ ). We observe instability only after many periods when we perturb the NLM along the eigenvector that is associated to the unstable Floquet multiplier  $\sigma \approx 1.007$ . See the top panel of Figure 7(b). However, if we initialize the dynamics with zero initial data, we approach and stay close to the NLM solution that we obtained via a Newton–Krylov method, even after 200 periods of motion. See the bottom panel of Figure 7(b). This suggests that solutions with weak instabilities can still attract nearby points in phase space, at least initially, and that our numerical prediction for  $f \approx 9.31$  Hz and  $a = 5.5$  mV is consistent with our experimental observations. Figure 7(c) is the same as Figure 7(a), but now the color scale corresponds to the magnitude of the maximum Floquet multiplier. This illustrates that the magnitude of the instability is weak throughout most of the solution branch. The instability has its largest growth rate (with  $\max(|\sigma_i|) \approx 2.15$ ) at the peak of the resonant curve. The onset of instability of the NLM with  $a = 5.5$  mV occurs due to a pair of complex conjugate Floquet multipliers that depart from the unit circle at approximately  $f = 9.31$  Hz. As the frequency decreases, additional multipliers depart from the unit circle. In Figure 7(d), we show the Floquet spectrum for  $f = 9.2$  Hz, indicating that there are purely real multipliers (corresponding to exponential growth) and complex multipliers (corresponding to oscillatory instabilities). Although we show only the principal branches of the NLMs in Fig. 7(a), it is possible that other bifurcations also occur. Indeed, the non-real nature of the Floquet multipliers that depart the unit circle suggest that there may be other types of solutions, such as quasiperiodic ones. We investigate this possibility in Sec. IV D. At smaller drive frequencies (within the pass band), the solutions on the main branch of NLMs can be stable. We do not investigate such solutions in depth, however, because they are spatially extended (and hence outside the scope of the present paper).

In Fig. 8(a), we show the gradual bending of the resonant peak for progressively larger excitation amplitudes with  $\phi = \pi/2$ . In particular, for  $a = 15$  mV, the peak bends so far that additional solutions emerge at  $f \approx 9.3$  Hz. However, these large-amplitude solutions are very unstable, and we were not able to access them either in our direct numerical simulations or in our experiments. Indeed, as we will discuss in Sec. IV D, we observe different types of dynamics at such excitation amplitudes. We can also tune the excitation angle  $\phi$  and thereby deform the resonant peak in a different way. For example, when we fix the excitation angle to  $\phi = 0$  (i.e., an excitation along  $n = 0$ ), the resonant curves are qualitatively similar to those for  $\phi = \pi/2$  for excitation amplitudes of  $a = 1$ ,  $a = 2$ , and  $a = 4$  [see Fig. 8(b)], although the stability properties are slightly different. For the large excitation of  $a = 15$  mV, the resonant curve bends even farther toward higher frequencies. Even greater qualitative differences occur for  $\phi = \pi/3$  (i.e., an excitation along  $m = 0$ ); see Fig. 8(c). In this case, for small-amplitude excitations, the resonant peak has a unimodal shape, as expected. However, as we consider gradually larger excitation amplitudes, an additional peak begins to emerge from the main solution branch, leading to a two-humped profile in the dependence of the RMS velocity on the frequency. This deformation is noticeable for relatively small excitation amplitudes. Specifically, we observe the existence of multiple solutions even for excitation amplitudes that are as small as  $a = 3$  mV, for which there is bifurcation at frequency  $f \approx 9.28$  Hz.

The frequency continuation with the excitation angle  $\phi = \pi/3$  is more representative of “typical” angles than the special

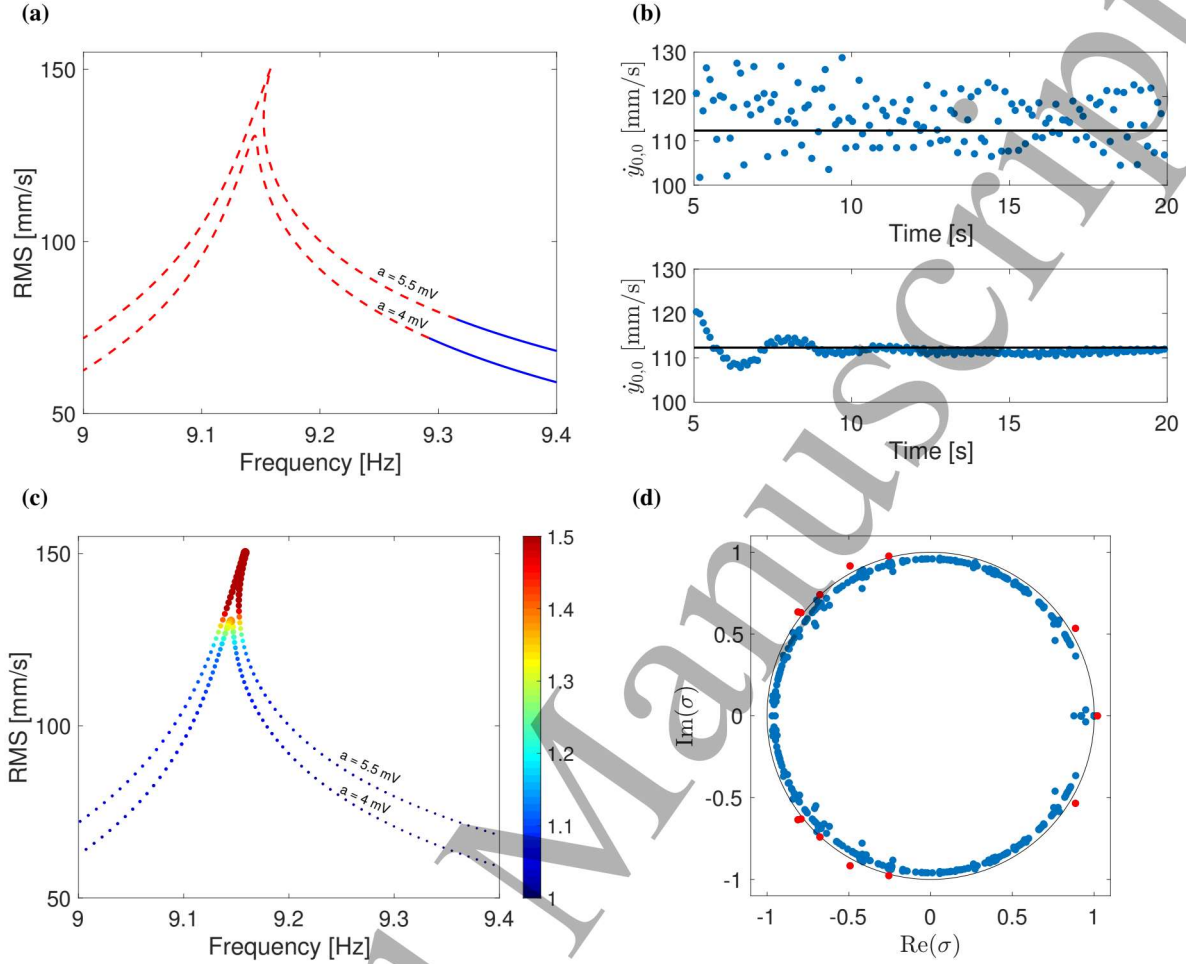


FIG. 7: Frequency continuation of NLMs. **(a)** Continuation with respect to frequency for a fixed excitation angle  $\phi = \pi/2$  for the two amplitudes,  $a = 4$  mV and  $a = 5.5$  mV, that we considered in Fig. 6. **(b)** In the top panel, we plot the local maxima of the time series of  $\dot{y}_{0,0}$  when we perturb the NLM with  $f = 9.3$  Hz and  $a = 5.5$  mV along the eigenvector that is associated with the largest-magnitude Floquet multiplier. The size of this perturbation is equal to 5% of the amplitude of the solution. The solid black line shows the corresponding value of the local maximum of the NLM that we obtain via a Newton–Krylov method. In the bottom panel, we plot local maxima of the time series when evolving zero initial data with a fixed frequency  $f = 9.3$  Hz and amplitude drive  $a = 5.5$ . **(c)** The same as panel (a), but with color intensity and disk radius corresponding to the magnitude of the largest Floquet multiplier (small blue disks are stable, whereas large red disks are unstable). The instabilities are fairly weak, except near the peaks of the resonant curves. **(d)** Floquet multipliers  $\sigma$  (markers) that are associated with the NLM at a drive frequency of  $f = 9.2$  Hz in the complex plane. We show the unit circle in gray. The presence of multipliers that lie outside the unit circle (red markers) indicate that this solution is unstable.

cases  $\phi = \pi/2$  and  $\phi = 0$ . For example, even by decreasing the angle slightly from  $\phi = \pi/2$  to  $\phi = 89\pi/180$ , we observe the additional branch in the frequency continuation [see Fig. 9(a)]. We show a plot of an NLM at frequency  $f = 9.2$  Hz that belongs to the main branch (i.e., the branch with smaller-amplitude NLMs) of the  $\phi = 89\pi/180$  continuation in Fig. 9(b). It has a similar profile to the NLM in Fig. 5. We show a plot of an NLM from the additional (i.e., larger-amplitude) branch at  $f = 9.2$  Hz in Fig. 9(c). The solutions along this branch have secondary amplitudes in the  $-\pi/3$  direction. It appears that the asymmetric nature of the drive is responsible for the excitation of this additional solution, whose profile is distinct from the solutions in the main branch.

#### D. Drive-Amplitude Sweeps

We now return to the effect of large-amplitude excitations for the parameter set — namely,  $\phi = \pi/2$  and  $f \approx 9.3$  Hz — in our laboratory experiments. Our bifurcation analysis revealed that the NLM solution at this parameter set destabilizes for larger amplitudes, although sometimes the instability is so weak that the NLMs are effectively stable on short enough time scales [see Fig. 7(b)]. We also observed that a large-amplitude branch of NLM solutions emerges at the parameter values  $\phi = \pi/2$  and

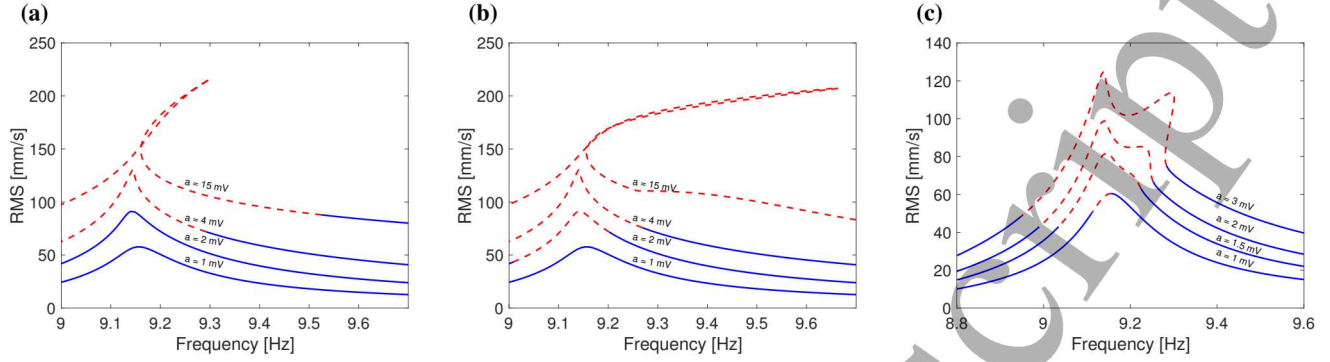


FIG. 8: **(a)** Frequency continuation with an excitation angle of  $\phi = \pi/2$  for excitation amplitudes  $a = 1$  mV,  $a = 2$  mV,  $a = 4$  mV, and  $a = 15$  mV. **(b)** Frequency continuation with  $\phi = 0$  for  $a = 1$  mV,  $a = 2$  mV,  $a = 4$  mV, and  $a = 15$  mV. Note that the curve corresponding to  $a = 15$  mV also crosses itself to form a loop, just like in panel (a). **(c)** Frequency continuation with  $\phi = \pi/3$  for  $a = 1$  mV,  $a = 1.5$  mV,  $a = 2$  mV, and  $a = 3$  mV.

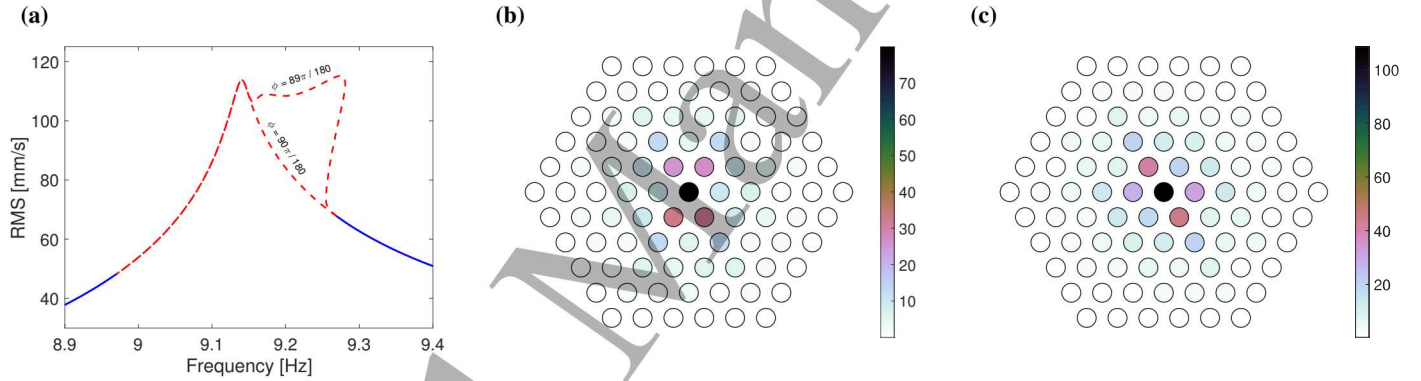


FIG. 9: **(a)** Frequency continuation with an excitation amplitude of  $a = 3$  mV for excitation angles of  $\phi = 89\pi/180$  and  $\phi = \pi/2$ . Our continuations for  $\phi = 89\pi/180$  and  $\phi = \pi/2$  are indistinguishable when we are outside the parameter region in which the  $\phi = 89\pi/180$  continuation has an additional branch of NLM solutions. **(b)** Profile of the NLM for  $f = 9.2$  Hz that belongs to the lower branch (i.e., the smaller-amplitude NLM branch) of the  $\phi = 89\pi/180$  continuation. **(c)** Profile of the NLM for  $f = 9.2$  Hz that belongs to the upper branch of the  $\phi = 89\pi/180$  continuation.

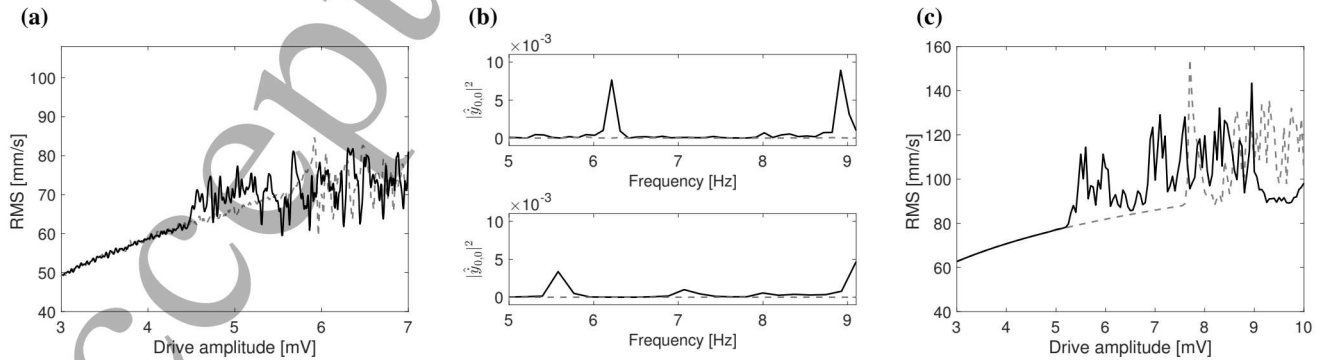


FIG. 10: **(a)** Our upswep (dashed gray curve) and downswep (solid black curve) of the drive amplitude  $a$  in our experiment. **(b)** The magnitude of the Fourier transform of the time series for the velocity of the center particle normalized by the height of the peak at  $f \approx 9.3$  Hz for (top panel) our experiment and (bottom panel) our numerical computation for an excitation amplitude  $a = 5.5$  mV. The dashed gray curve is the small-amplitude state (in the form of an NLM) that we obtain from the upswep, and the solid black curve is the large-amplitude state that we obtain from the downswep. **(c)** The upswep (dashed gray curve) and downswep (solid black curve) of the amplitude in our numerical simulations.

$f \approx 9.3$  Hz for sufficiently large excitation amplitudes [see Fig. 8(a)].

To study the dynamics at larger amplitudes in experiments, we initialize the system with a small-amplitude excitation (of  $a = 1$  mV) and gradually increase the amplitude in increments of 0.05 mV. For each step, we run the system for 90 periods, which allows sufficient time to settle to a steady state if there is one. We record the RMS of the velocity of the center magnet for the final 5 seconds. We call this procedure an amplitude “upsweep”. We use an analogous procedure when we start with a large excitation amplitude, which we gradually decrease in steps of size 0.05 mV. We call this procedure an amplitude “downsweep”. We show our experimental results for the upsweep and downsweep in Fig. 10(a). For sufficiently small amplitudes (specifically, for  $a \lesssim 4.5$  mV) both the upsweep and downsweep approach the same NLM, suggesting that there is a single stable branch of NLMs for  $a \lesssim 4.5$  mV. However, for  $a \gtrsim 4.5$  mV, there appear to be two different states; we obtain the small-amplitude states when we perform an upsweep and the large-amplitude states when we perform a downsweep. The small-amplitude states have the form of an NLM. The experimental result in Fig. 6(b) is an example of the small-amplitude state for  $a = 5.5$  mV. The large-amplitude states are also localized, but they are no longer periodic in time. An inspection of the Fourier transform of the large-amplitude state for  $a = 5.5$  mV reveals other peaks in the spectrum (in addition to a peak at the excitation frequency  $f \approx 9.3$  Hz). In the top panel of Fig. 10(b), we show the Fourier transform of both the large-amplitude state and the small-amplitude state. The small-amplitude state (i.e., the NLM) has no peaks for lower frequencies, whereas the large-amplitude state has peaks at approximately  $f = 8.9$  Hz and  $f = 6.2$  Hz; this is suggestive of quasiperiodic behavior.

We obtain qualitatively similar results when we perform analogous upsweeps and downsweeps in numerical computations. We also observe the emergence of two states in these computations [see Fig. 10(c)]. In our computations, the large-amplitude state departs from the branch of NLMs for excitation amplitudes that are slightly larger (specifically, for  $a \gtrsim 5.1$  mV) than in our experiments. The amplitude  $a \approx 5.1$  mV is roughly where the numerical NLM branch destabilizes. As in our experiments, these large-amplitude states are not periodic in time. One can also observe the presence of secondary peaks in their Fourier transforms in our numerical solutions, although the locations of these peaks are slightly different than in our experiments. See the bottom panel of Fig. 10(b). Although these numerical large-amplitude states have features that are similar to those of time-quasiperiodic states (given the multiple incommensurate peaks in the Fourier transform), it is also possible that these large-amplitude states are weakly chaotic. One issue is that we were unable to detect asymptotically stable time-quasiperiodic orbits for parameter values that correspond to the experiments. If such solutions were attractors, it would be straightforward to determine if the large-amplitude states are time-quasiperiodic ones by plotting Poincaré sections of the orbits.

To clarify the nature of the large-amplitude states, we modify the parameter values slightly to obtain stable time-quasiperiodic solutions. We perform amplitude upsweeps and downsweeps for the parameter set  $\phi = \pi/2$ ,  $f = 9.65$  Hz, and  $M_b = 125$  g. We use a different drive frequency from our prior calculations, because the smaller mass  $M_b = 125$  g leads to a cutoff frequency of  $f_c \approx 9.01$  Hz and a defect frequency of  $f_d \approx 9.36$  Hz. The amplitude sweeps with these parameter values lead to a well-defined large-amplitude branch of solutions that bifurcates from the main branch of periodic ones (the NLMs) [see Fig. 11(a)]. In Fig. 11(a), we show three solid markers to point out the locations of three solutions: a large-amplitude state that appears to be either time-quasiperiodic or time-chaotic in black, the NLM (in gray), and a stable time-quasiperiodic orbit (in red). We show a plot of a projection of the Poincaré section in the  $(y, \dot{y})$  plane in Fig. 11(b) for the two states that are not time-periodic. The orbit in the bottom panel reveals a well-defined invariant curve, illustrating the quasiperiodic nature of the solution. We show the Fourier transforms of these two non-periodic states in Fig. 11(c). Both have a secondary peak in the spectrum, demonstrating that the solutions are indeed non-periodic in time (because of the incommensurate peaks in the frequency spectra). Laboratory experiments for this modified parameter set yield similar results. In particular, there is a well-defined large-amplitude branch of solutions that bifurcates from a branch of time-periodic solutions [see Fig. 11(d,e)]. The Fourier transform of one of the large-amplitude states also has a secondary peak in the spectrum, an indication that the state is nearly quasiperiodic. For simplicity, we henceforth use the term “quasiperiodic” for such a state.

Because the numerical computations and experiments with the mass  $M_b = 125$  g reveal the existence of time-quasiperiodic orbits that bifurcate from the main branch of time-periodic NLMs, it is reasonable to conclude that these quasiperiodic solutions persist when we continue the parameters to the original parameter set  $M_b = 138.2$  g and  $f_d = 9.3$ . This suggests that the large-amplitude branch in Fig. 10(a,c) consists of time-quasiperiodic solutions.

## V. CONCLUSIONS

We have demonstrated, both experimentally and numerically, the existence of nonlinear localized modes in a 2D hexagonal lattice of repelling magnets. By exploring the effects of nonlinearity numerically using frequency continuation and experimentally using amplitude sweeps, we revealed the emergence of both time-periodic NLMs and time-quasiperiodic localized states. We have also established that our experimental setup is a viable approach for fundamental studies in nonlinear lattice systems that go beyond what can occur in 1D chains. We found that the smaller-amplitude NLMs that we considered are stable, whereas progressively larger excitation amplitudes led to instabilities and more complicated dynamics, including time-quasiperiodic and potentially time-chaotic behavior. We also explored the anisotropy of the hexagonal lattice by considering different excitation angles and examining the nature and decay of the states along these angles.

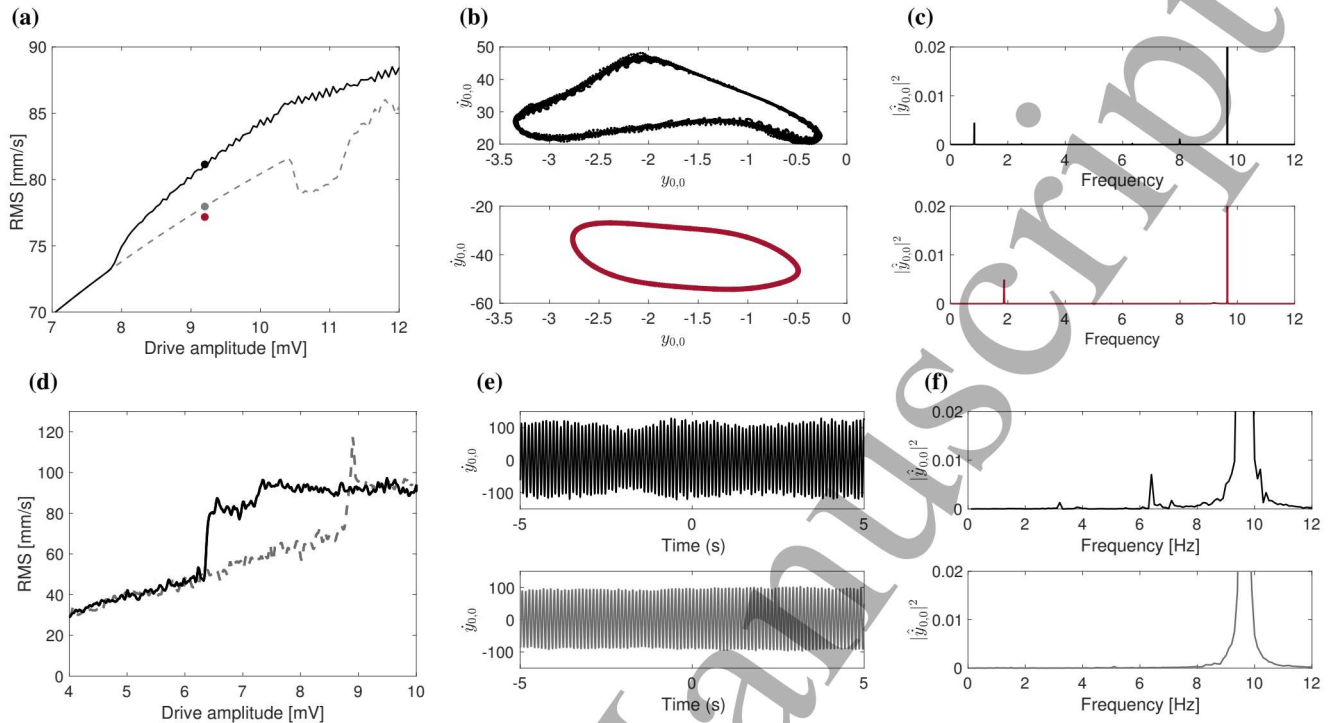


FIG. 11: (a) The upswep (dashed gray curve) and downswep (solid black curve) for our numerical simulations with  $M_b = 125$  g and  $f = 9.65$  Hz. Three states exist when we use an excitation amplitude of  $a = 9.2$  mV. Two of the states (the black and red dots) are not periodic in time, and the other state (the gray dot) is time-periodic. We obtain the state that is indicated by the red dot by simulating zero initial data for 90 periods of motion. (b) In the top panel, we show a projection of the Poincaré section of the solution that is represented by the black dot in panel (a). In the bottom panel, we show a projection of the Poincaré section of the solution that is represented by the red dot in panel (a). (c) The magnitudes of the Fourier transforms of the solutions in panel (b). (d) The upswep (dashed gray curve) and downswep (solid black curve) for our experiments. (e) The gray curve is the experimental time series of the small-amplitude state that we obtain from the upswep for an excitation amplitude of  $a = 8$  mV. The solid black curve is the time series of the large-amplitude state that we obtain from the downswep for an excitation amplitude of  $a = 8$  mV. (f) The magnitude of the Fourier transform of the time series of panel (e) normalized by the height of the peak at  $f = 9.5$ . The gray curve corresponds to the small-amplitude state, and the solid black curve corresponds to the large-amplitude state.

Our work paves the way for many future studies. For example, although our parameter continuation in frequency revealed several families of solutions, there are undoubtedly — given the complexity of the studied system — several other ones (including possibly exotic ones) to discover. Other avenues of future work include the study of refined models — such as ones that account for nonlinear damping (or, more generally, a more elaborate form of damping [47–49]), rotational effects (which can be rather important [50, 51]), and/or long-range interactions [38] — of our lattice system. Each of these aspects will add elements of complexity, but they also may lead to other types of interesting dynamics, such as the possibility of breather solutions with algebraically decaying tails in space [38, 39]. It is also possible that the inclusion of rotational effects and/or more sophisticated damping models may help improve matches with laboratory experiments. Such models have an associated cost of being more complicated and hence more cumbersome to analyze and simulate. Our attempt in the present paper has been to explore the principal features of the interplay of discreteness, local disorder, and nonlinearity in a hexagonal lattice of magnets. Breathers in heterogeneous hexagonal magnetic lattices (e.g., ones with a repeating pattern of two masses) may lead to the existence of intrinsic localized modes and are also worthy of future study. In that context, the study of band gaps, instabilities, and nonlinear modes and their propagation is another topic of substantial ongoing interest.

### Acknowledgements

The present paper is based on work that was supported by the US National Science Foundation under Grant Nos. DMS-1615037 (CC), DMS-1809074 (PGK), and EFRI-1741565 (CD). AJM acknowledges support from the Agencia Nacional de Investigación y Desarrollo de Chile (ANID) under Grant No. 3190906. EGC thanks Bowdoin College, where the initial stages of this work were carried out, for their kind hospitality. PGK also acknowledges support from the Leverhulme Trust via a Visiting Fellowship and thanks the Mathematical Institute of the University of Oxford for its hospitality during part of this work.

We give special thanks to Bowdoin undergraduates Ariel Gonzales, Patrycja Pekala, Anam Shah, and Steven Xu for help with simulations and data management.

## Appendix

**Derivation of the external force from the wire:** To derive the external force that the wire exerts on a magnet, we first define our coordinate system. We choose a set of orthogonal unit vectors  $\hat{r}$ ,  $\hat{z}$ , and  $\hat{s}$  that are centered on the wire and oriented such that the wire is aligned with the  $\hat{s}$  axis [see Fig. 12(a)]. We model the magnetic moment  $\mu$  of the magnet using the Gilbert model of a magnetic dipole [52]:

$$\mathbf{F}_{\text{wire}} = (\mu \cdot \nabla) \mathbf{B}, \quad (15)$$

which describes the force that acts on the dipole due to the magnetic field  $\mathbf{B}$ . In our setup, the wire carries an electric current  $I$  that generates the magnetic field  $\mathbf{B}(r, z) = B_r(r, z)\hat{r} + B_z(r, z)\hat{z}$ . Evaluating  $\mathbf{B}$  at the position  $-h\hat{z} + r\hat{r}$  of the magnet yields

$$\mathbf{B}(r, -h) = \frac{I\mu_0}{2\pi\sqrt{h^2 + r^2}} (\sin\theta \hat{r} + \cos\theta \hat{z}), \quad (16)$$

where  $\mu_0$  is the magnetic permeability and  $\theta$  is the angle between  $\mathbf{B}$  and  $\mu$ . We are assuming that we can neglect the dynamics along the  $\hat{z}$  axis, so we are interested only in the  $\hat{r}$  component of the force. Inserting Eq. (16) into Eq. (15) and taking  $\mu = \mathcal{M}\hat{z}$ , we obtain

$$\mathbf{F}_{\text{wire}} = \mathcal{M} \partial_r B_z(r, z) \hat{r} = \frac{I\mu_0 \mathcal{M}}{2\pi} \frac{h^2 - r^2}{(h^2 + r^2)^2} \hat{r}, \quad (17)$$

which corresponds to Eq. (1). In our coordinates, we place the wire in an orientation in the plane that is spanned by the lattice basis vectors  $e_1 = (1, 0)$  and  $e_2 = (1/2, \sqrt{3}/2)$ . However, it is straightforward to write Eq. (17) in coordinates in the  $\{e_1, e_2\}$  basis by including a parameter  $\phi$  that accounts for the excitation angle. For instance, for the central magnet, we may write

$$\mathbf{F}_{0,0}^{\text{ext}} = \frac{I\mu_0 \mathcal{M}}{2\pi} \begin{pmatrix} \cos(\phi) \frac{h^2 - x_{0,0}^2}{(h^2 + x_{0,0}^2)^2} \\ \sin(\phi) \frac{h^2 - y_{0,0}^2}{(h^2 + y_{0,0}^2)^2} \end{pmatrix}, \quad (18)$$

which corresponds to Eq. (4).

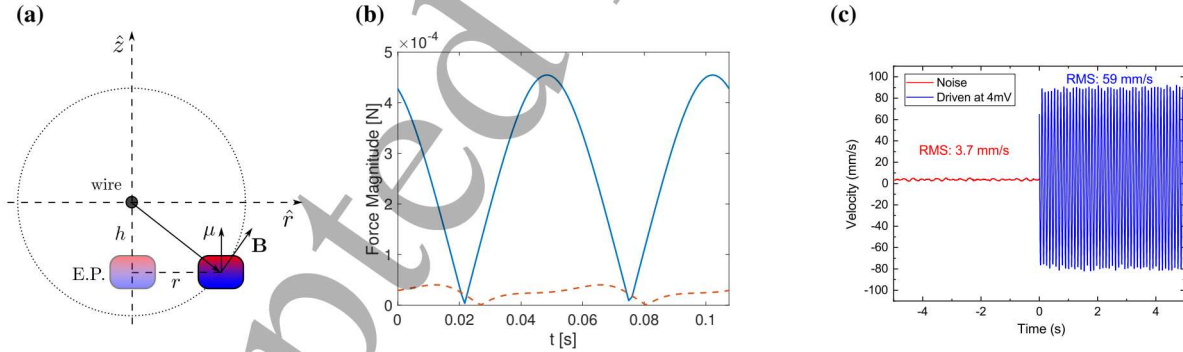


FIG. 12: **(a)** Schematic illustration of the interaction between a single magnet and a wire in the  $(\hat{r}, \hat{z})$  plane, which is orthogonal to the direction of the wire. We use “E.P.” to denote the static-equilibrium position of the magnet. **(b)** Squared magnitudes of the forces that result from lattice interactions (solid blue curve) and the external drive from the wire (dashed red curve) for the NLM from Fig. 5(a) during one period of motion. Specifically, we plot  $|\mathbf{F}_{0,0}^{\text{lattice}}(t)|^2$  using the solid blue curve and  $|\mathbf{F}_{0,0}^{\text{ext}}(t)|^2$  using the dashed red curve. **(c)** The experimentally measured velocity time series of the center unit in the undriven lattice (i.e., the background noise, which we show in the red curve on the left) and after stabilization when we drive it at  $a = 4$  mV and  $f = 9.3$  Hz (the blue curve on the right). We use the RMS of the noise to estimate the noise level in Fig. 6.

**Comparison of external and internal nonlinear forces:** Although the form of the force that describes the external drive is specific to our experimental setup, the dynamics are dominated by the lattice forces. For example, in Fig. 12(b), we compare the forces that result from the wire (see Eq. (18)) and the force from the lattice for the NLM of Fig. 5(a). The lattice forces are

$$\begin{aligned} \mathbf{F}_{m,n}^{\text{lattice}} = & -\mathbf{F}_0(\mathbf{q}_{m+1,n} - \mathbf{q}_{m,n}) - \mathbf{F}_1(\mathbf{q}_{m,n+1} - \mathbf{q}_{m,n}) + \mathbf{F}_{-1}(\mathbf{q}_{m,n} - \mathbf{q}_{m-1,n+1}) \\ & + \mathbf{F}_0(\mathbf{q}_{m,n} - \mathbf{q}_{m-1,n}) + \mathbf{F}_1(\mathbf{q}_{m,n} - \mathbf{q}_{m,n-1}) - \mathbf{F}_{-1}(\mathbf{q}_{m+1,n-1} - \mathbf{q}_{m,n}). \end{aligned} \quad (19)$$

However, it is important to acknowledge that the effective “defect” that is produced by the force (19) is responsible for the presence of the corresponding linear defect frequency and hence for the associated NLMs in the presence of nonlinearity.

**Noise Estimation:** Even if we do not apply an external drive to the lattice, the particles still exhibit detectable motion. This is due to interactions with the air flow from the table and to imperfections (e.g., nonaxisymmetric mass distributions) of the particles. To estimate the noise floor of the system, we measure the velocity time series of the center particle is when there is no drive. The corresponding RMS velocity is the noise estimation. We find that the RMS velocity of the noise is 6% of the RMS velocity of the system when we drive it at 4mV [see Fig. 12(c)].

- 
- [1] F. Lederer, G. I. Stegeman, D. N. Christodoulides, G. Assanto, M. Segev, and Y. Silberberg, “Discrete solitons in optics,” *Phys. Rep.*, vol. 463, p. 1, 2008.
  - [2] P. Binder, D. Abraimov, A. V. Ustinov, S. Flach, and Y. Zolotaryuk, “Observation of breathers in Josephson ladders,” *Phys. Rev. Lett.*, vol. 84, p. 745, 2000.
  - [3] E. Trías, J. J. Mazo, and T. P. Orlando, “Discrete breathers in nonlinear lattices: Experimental detection in a Josephson array,” *Phys. Rev. Lett.*, vol. 84, p. 741, 2000.
  - [4] L. Q. English, M. Sato, and A. J. Sievers, “Modulational instability of nonlinear spin waves in easy-axis antiferromagnetic chains. II. influence of sample shape on intrinsic localized modes and dynamic spin defects,” *Phys. Rev. B*, vol. 67, p. 024403, 2003.
  - [5] U. T. Schwarz, L. Q. English, and A. J. Sievers, “Experimental generation and observation of intrinsic localized spin wave modes in an antiferromagnet,” *Phys. Rev. Lett.*, vol. 83, p. 223, 1999.
  - [6] B. I. Swanson, J. A. Brozik, S. P. Love, G. F. Strouse, A. P. Shreve, A. R. Bishop, W.-Z. Wang, and M. I. Salkola, “Observation of intrinsically localized modes in a discrete low-dimensional material,” *Phys. Rev. Lett.*, vol. 82, p. 3288, 1999.
  - [7] M. Peyrard, “Nonlinear dynamics and statistical physics of DNA,” *Nonlinearity*, vol. 17, p. R1, 2004.
  - [8] J. Bajars, J. C. Eilbeck, and B. Leimkuhler, *Numerical Simulations of Nonlinear Modes in Mica: Past, Present and Future*, vol. 221, p. 35. Cham, Switzerland: Springer International Publishing, 2015.
  - [9] O. Morsch and M. Oberthaler, “Dynamics of Bose–Einstein condensates in optical lattices,” *Rev. Mod. Phys.*, vol. 78, p. 179, 2006.
  - [10] S. Flach and A. Gorbach, “Discrete breathers: Advances in theory and applications,” *Phys. Rep.*, vol. 467, p. 1, 2008.
  - [11] P. G. Kevrekidis, “Non-linear waves in lattices: Past, present, future,” *IMA J. Appl. Math.*, vol. 76, pp. 389–423, 2011.
  - [12] S. V. Dmitriev, E. A. Korznikova, Y. A. Baimova, and M. G. Velarde, “Discrete breathers in crystals,” *Physics-Uspokhi*, vol. 59, pp. 446–461, may 2016.
  - [13] E. Fermi, J. Pasta, and S. Ulam, “Studies of Nonlinear Problems. I,” (*Los Alamos National Laboratory, Los Alamos, NM, USA*), vol. Tech. Rep., pp. LA–1940, 1955.
  - [14] G. Gallavotti, *The Fermi–Pasta–Ulam Problem: A Status Report*. Heidelberg, Germany: Springer-Verlag, 2008.
  - [15] V. F. Nesterenko, *Dynamics of Heterogeneous Materials*. Heidelberg, Germany: Springer-Verlag, 2001.
  - [16] C. Chong and P. G. Kevrekidis, *Coherent Structures in Granular Crystals: From Experiment and Modelling to Computation and Mathematical Analysis*. Heidelberg, Germany: Springer-Verlag, 2018.
  - [17] Y. Starosvetsky, K. R. Jayaprakash, M. A. Hasan, and A. F. Vakakis, *Topics On The Nonlinear Dynamics And Acoustics Of Ordered Granular Media*. World Scientific, Singapore, 2017.
  - [18] C. Chong, M. A. Porter, P. G. Kevrekidis, and C. Daraio, “Nonlinear coherent structures in granular crystals,” *J. Phys. Cond. Matt.*, vol. 29, p. 413003, 2017.
  - [19] M. Molerón, A. Leonard, and C. Daraio, “Solitary waves in a chain of repelling magnets,” *J. App. Phys.*, vol. 115, no. 18, p. 184901, 2014.
  - [20] A. Mehrem, N. Jiménez, L. J. Salmerón-Contreras, X. García-Andrés, L. M. García-Raffi, R. Picó, and V. J. Sánchez-Morcillo, “Nonlinear dispersive waves in repulsive lattices,” *Phys. Rev. E*, vol. 96, p. 012208, 2017.
  - [21] M. Serra-Garcia, M. Molerón, and C. Daraio, “Tunable, synchronized frequency down-conversion in magnetic lattices with defects,” *Phil. Trans. Roy. Soc. A: Math. Phys. Eng. Sci.*, vol. 376, no. 2127, p. 20170137, 2018.
  - [22] J. L. Marín, J. C. Eilbeck, and F. M. Russell, “Localized moving breathers in a 2D hexagonal lattice,” *Phys. Lett. A*, vol. 248, no. 2, pp. 225–229, 1998.
  - [23] J. L. Marín, J. C. Eilbeck, and F. M. Russell, *2-D Breathers and Applications*, vol. 542, p. 293. Heidelberg, Germany: Springer-Verlag, 2000.
  - [24] L. Q. English, F. Palmero, J. F. Stormes, J. Cuevas, R. Carretero-González, and P. G. Kevrekidis, “Nonlinear localized modes in two-dimensional electrical lattices,” *Phys. Rev. E*, vol. 88, p. 022912, 2013.
  - [25] S. Vladimirov and K. Ostrikov, “Dynamic self-organization phenomena in complex ionized gas systems: New paradigms and technological aspects,” *Phys. Rep.*, vol. 393, no. 3, pp. 175–380, 2004.
  - [26] V. Koukoulouyannis, P. G. Kevrekidis, K. J. H. Law, I. Kourakis, and D. J. Frantzeskakis, “Existence and stability of multisite breathers in honeycomb and hexagonal lattices,” *J. Phys. A: Math. Theor.*, vol. 43, no. 23, p. 235101, 2010.
  - [27] J. A. D. Wattis, *Asymptotic Approximation of Discrete Breather Modes in Two-Dimensional Lattices*, vol. 221, p. 179. Heidelberg, Germany: Springer-Verlag, 2015.
  - [28] S. Flach, K. Kladko, and S. Takeno, “Acoustic breathers in two-dimensional lattices,” *Phys. Rev. Lett.*, vol. 79, pp. 4838–4841, 1997.
  - [29] B.-B. Lü and T. Qiang, “Discrete gap breathers in a two-dimensional diatomic face-centered square lattice,” *Chinese Physics B*, vol. 18, no. 10, p. 4393, 2009.

- [30] V. Koukouloyannis and I. Kourakis, “Discrete breathers in hexagonal dusty plasma lattices,” *Phys. Rev. E*, vol. 80, p. 026402, 2009.
- [31] B.-F. Feng and T. Kawahara, “Discrete breathers in two-dimensional nonlinear lattices,” *Wave Motion*, vol. 45, no. 1, pp. 68 – 82, 2007.
- [32] A. A. Maradudin, E. W. Montroll, and G. H. Weiss, *Theory of Lattice Dynamics in the Harmonic Approximation*. New York City, NY, USA: Academic Press, 1963.
- [33] G. Theocharis, M. Kavousanakis, P. G. Kevrekidis, C. Daraio, M. A. Porter, and I. G. Kevrekidis, “Localized breathing modes in granular crystals with defects,” *Phys. Rev. E*, vol. 80, p. 066601, 2009.
- [34] P. Bowcock, E. Corrigan, and C. Zambon, “Some aspects of jump-defects in the quantum sine-gordon model,” *Journal of High Energy Physics*, vol. 2005, no. 08, pp. 023–023, 2005.
- [35] N. Boechler, G. Theocharis, and C. Daraio, “Bifurcation based acoustic switching and rectification,” *Nat. Mater.*, vol. 10, no. 9, p. 665, 2011.
- [36] C. Hoogeboom, Y. Man, N. Boechler, G. Theocharis, P. G. Kevrekidis, I. G. Kevrekidis, and C. Daraio, “Hysteresis loops and multi-stability: From periodic orbits to chaotic dynamics (and back) in diatomic granular crystals,” *Euro. Phys. Lett.*, vol. 101, p. 44003, 2013.
- [37] C. Chong, A. Foehr, E. G. Charalampidis, P. G. Kevrekidis, and C. Daraio, “Breathers and other time-periodic solutions in an array of cantilevers decorated with magnets,” *Math. Eng.*, vol. 1, pp. 489–507, 2019.
- [38] M. Molerón, C. Chong, A. J. Martínez, M. A. Porter, P. G. Kevrekidis, and C. Daraio, “Nonlinear excitations in magnetic lattices with long-range interactions,” *New J. Phys.*, vol. 21, p. 063032, 2019.
- [39] S. Flach, “Breathers on lattices with long range interaction,” *Phys. Rev. E*, vol. 58, pp. R4116–R4119, 1998.
- [40] R. F. Steidel, *An Introduction to Mechanical Vibrations*. New York City, NY, USA: John Wiley & Sons, Inc., 1989.
- [41] M. Lepidi, “Multi-parameter perturbation methods for the eigensolution sensitivity analysis of nearly-resonant non-defective multi-degree-of-freedom systems,” *Journal of Sound and Vibration*, vol. 332, no. 4, pp. 1011–1032, 2013.
- [42] C. T. Kelley, *Solving Nonlinear Equations with Newton’s Method*. Philadelphia, PA, USA: Society for Industrial and Applied Mathematics, 2003.
- [43] E. Doedel and L. S. Tuckerman, *Numerical Methods for Bifurcation Problems and Large-Scale Dynamical Systems*. Heidelberg, Germany: Springer-Verlag, 2000.
- [44] M. W. Hirsch, S. Smale, and R. L. Devaney, *Differential Equations, Dynamical Systems, and an Introduction to Chaos*. Amsterdam, The Netherlands: Elsevier, 2004.
- [45] B. A. Malomed, “Potential of interaction between two- and three-dimensional solitons,” *Phys. Rev. E*, vol. 58, pp. 7928–7933, Dec 1998.
- [46] R. J. Decker, A. Demirkaya, N. S. Manton, and P. G. Kevrekidis, “Kink–antikink interaction forces and bound states in a biharmonic  $\phi^4$  model,” *arXiv:2005.04523*, 2020.
- [47] A. Rosas, A. H. Romero, V. F. Nesterenko, and K. Lindenberg, “Observation of two-wave structure in strongly nonlinear dissipative granular chains,” *Phys. Rev. Lett.*, vol. 98, p. 164301, 2007.
- [48] L. Vergara, “Model for dissipative highly nonlinear waves in dry granular systems,” *Phys. Rev. Lett.*, vol. 104, p. 118001, 2010.
- [49] R. Carretero-González, D. Khatri, M. A. Porter, P. G. Kevrekidis, and C. Daraio, “Dissipative solitary waves in granular crystals,” *Phys. Rev. Lett.*, vol. 102, p. 024102, 2009.
- [50] A. Merkel, V. Tournat, and V. Gusev, “Experimental evidence of rotational elastic waves in granular phononic crystals,” *Phys. Rev. Lett.*, vol. 107, p. 225502, 2011.
- [51] K. Vorotnikov, M. Kovaleva, and Y. Starosvetsky, “Emergence of non-stationary regimes in one- and two-dimensional models with internal rotators,” *Phil. Trans. A: Math. Phys. Eng. Sci.*, vol. 376, p. 20170134, 2018.
- [52] J. D. Jackson, *Classical Electrodynamics*. New York City, NY, USA: John Wiley & Sons, Inc., 3rd ed. ed., 1999.